

## Cooling curve and microchemical phase analysis of rapidly quenched magnesium AM60B and AE44 alloys

A.J. Gesing <sup>a</sup>, J.H. Sokolowski <sup>b,\*</sup>, P.C. Marchwica <sup>b</sup>, C. Blawert <sup>c</sup>,  
J. Jekl <sup>d</sup>, M. Kozdras <sup>e</sup>, M. Kasprzak <sup>f</sup>, J. Wood <sup>g</sup>

<sup>a</sup> Gesing Consultants Inc., Tecumseh, ON, Canada; <sup>b</sup> University of Windsor, Windsor, ON, Canada; <sup>c</sup> Helmholtz-Zentrum Geesthacht Zentrum für Material und Küstenforschung GmbH, Geesthacht, Germany; <sup>d</sup> Meridian Lightweight Technologies Inc., Strathroy, ON, Canada; <sup>e</sup> Canmet MATERIALS-Materials Technology Lab, Natural Resources Canada, Hamilton, ON, Canada; <sup>f</sup> Silesian University of Technology, Gliwice, Poland; <sup>g</sup> University of Western Ontario, London, ON, Canada

\* Corresponding e-mail address: jerry@uwindsor.ca

Received 10.03.2013; published in revised form 01.06.2013

### Materials

#### ABSTRACT

**Purpose:** Development of the understanding of the effect of the solidification rate with the alloy microstructures for the structural AM60B and the creep resistant AE44 Mg casting alloys.

**Design/methodology/approach:** Tubular macro test samples of magnesium alloys AM60B and AE44 were melted and quenched at maximum instantaneous cooling rates ranging from -5°C/s to -500°C/s in the Universal Metallurgical Simulator and Analyzer (UMSA) Technology Platform while recording the temperature-time traces. Such rapid cooling rates are typical in water-cooled dies used in high pressure die casting (HPDC). Characteristic reactions on these curves corresponding to the formation of individual phases during solidification were quantified based on cooling curve analysis combined with metallographic and micro-chemical analysis, with the aid of literature data.

**Findings:** The results indicate that these phases, their size and location in the microstructure, their chemistry and their relative proportions all change in response to the increase in the cooling rate. The results are drastically different for the two alloy systems studied. Solidification of AM60B alloy yields small, equiaxed  $\alpha$ -Mg rosettes whose size is mostly independent of the cooling rate. These rosettes nucleate heterogeneously on Al<sub>18</sub>Mn<sub>5</sub> phases that are first to form, and are surrounded by the eutectic structure of Mg and Mg<sub>17</sub>Al<sub>12</sub>. In contrast, the AE44 has very large  $\alpha$ -Mg grains at all cooling rates. These grains are filled with Al<sub>11</sub>RE<sub>3</sub> platelets or dendrites. Results suggest that the Al<sub>11</sub>RE<sub>3</sub> phase is completely ineffective in heterogeneous nucleation of  $\alpha$ -Mg grains.

**Originality/value:** In this research the authors significantly extended the thermal analysis methodology. The specific results obtained on the structural and creep-resistant Mg casting alloys are of significant value to the development of automotive light metal structures and power train components as well as further development of solidification codes for the commercial HPDC process.

**Keywords:** AM60; AE44; Magnesium; Thermal analysis; Micro-chemical analysis

#### Reference to this paper should be given in the following way:

A.J. Gesing, J.H. Sokolowski, P.C. Marchwica, C. Blawert, J. Jekl, M. Kozdras, M. Kasprzak, J. Wood, Cooling curve and microchemical phase analysis of rapidly quenched magnesium AM60B and AE44 alloys, Journal of Achievements in Materials and Manufacturing Engineering 58/2 (2013) 59-73.

## 1. Introduction

With low density and good mechanical properties, magnesium alloys are increasingly being adopted for use in the automotive industry. As lightweight structural materials they feature excellent ductility, castability and strength and are currently being used for such components as instrument panels, seat frames and steering wheels [1-3]. Many magnesium alloys, such as AE44 and AM60B, have been developed in order to obtain specific ranges of properties. AE44, an alloy with additions of aluminum and rare earth (RE) elements, is used for its good high temperature mechanical properties and corrosion resistance [4]. AM60B, with additions of aluminum and manganese, has good energy absorption characteristics and ductility [5].

High Pressure Die Casting is the predominant forming method for Mg based alloys. Large markets for such die cast alloys include portable consumer electronic housings and automotive/aerospace components. These applications involve use at ambient temperature. Other uses such as engine components expose the alloy to elevated temperatures and thus require higher temperature strength and creep resistance. AM60B is a general purpose die casting alloy containing ~6% Al and >0.3% Mn (wt. %). Intended for ambient temperature applications, AM60B is designed for low cost, low density, good castability, and room temperature strength and improved ductility over the industry workhorse AZ91D alloy.

In AM60B, the addition of Al improves the castability by providing the  $Mg_{17}Al_{12}$  intermetallic phase, which preserves fluidity during casting until a low temperature (~400°C) eutectic reaction with Mg occurs. Mn has a high affinity for impurities such as Fe and Ni (which lead to electrochemical corrosion) and traps them in  $Al_8Mn_5$  intermetallic precipitates. Under thermodynamic equilibrium, these precipitates form in liquid Mg just above its melting point of 650°C and can be removed with additional melt treatment. Without melt treatment, these precipitates can provide nucleation sites for the solidification of primary  $\alpha$ Mg grains. Such nucleation promotes reduction of grain size and thus contributes to the improvement in strength and ductility.

AE44 is among alloys being considered for elevated temperature engine component applications. It contains ~4% Al and ~4% RE element mischmetal containing Ce, La, Nd and smaller amounts of other RE elements. It sacrifices solidification range in exchange for high temperature phase and microstructural stability, which translates to retention of strength and high creep resistance over extended use times.

RE metals have similar valence electron shells and thus similar chemical behaviour. They are often found together and upon reduction and refining form mischmetal. In spite of being called 'rare,' their abundance is similar to Ni and Co and RE metals are suitable as alloying element additions for alloys used in large-scale markets such as automotive and aerospace where improved high temperature mechanical performance is required [6].

RE metals form similar intermetallic crystal structures when bonded with Al as  $Al_{11}RE_3$  or  $Al_3RE$ . Ce, La, Nd, Pr and Gd substitute freely on the RE sites in the intermetallic crystal. The result is that a Mg-Al-RE mischmetal system behaves similarly to a ternary alloy system forming few intermetallic phases. Furthermore, there is very high chemical affinity between Al and the REs. This reduces Al activity in the liquid alloy and

suppresses formation of intermetallic phases typically found in the Al-Mg-X systems. Al-RE intermetallics form at temperatures very close to the liquidus temperature of  $\alpha$ Mg and by consuming the Al from the liquid they drastically reduce the solidification range compared to what would be expected for a Mg alloy containing 4% Al alone.

## 2. Experimental

### 2.1. Solidification

The Universal Metallurgical Simulator and Analyzer (UMSA) Technology Platform [7] is a desktop thermal analysis system capable of simulating various foundry processes in a quick and cost effective manner. The basic platform function is heating samples using an induction coil and recording in-situ temperature changes using a thermocouple connected to a data acquisition system. The platform is also applicable for testing other process parameters including cooling/heat treatment cycles and the effects of vacuum or controlled gaseous environments. Recent developments of the platform have focused on improving the quenching capabilities in order to simulate higher cooling rates. While the previous platform was capable of reaching instantaneous cooling rates of around -30°C/s while blowing cold gas at the outer surface of an 18-mm diameter solid cylindrical sample, the latest changes increase cooling rate capabilities to -500°C/s for macro test samples. The faster cooling rates are enabled by the use of hollow test samples that accommodate a central cooling channel, increase the surface-area-to-volume ratio and allow for the use of liquid coolants.

The alloys used in these experiments (AM60B and AE44) were provided by Meridian Technologies Inc. in the form of ingots. Nominally pure magnesium was provided in the form of bar stock. Hollow test samples were cut from the raw material with dimensions (12 × 18 × 23 mm (ID × OD × L)) with an additional hole placed within the wall to accommodate the thermocouple. K-type thermocouples (~0.5mm OD) were used in the experiments. Thermocouple calibration was performed using an RTD probe. All samples were coated in colloidal graphite and placed in low thermal mass stainless steel foil crucibles. The thermocouple was also coated in graphite prior to insertion into the sample. Experimental conditions and process parameters were maintained constant throughout the course of the study. These include holding time, holding temperature, heating rate and atmosphere (argon).

In order to investigate capabilities of the modified UMSA platform, experiments were performed using various combinations of alloy and cooling methods. Each sample in the study was assigned to a particular cooling method and subjected to three repeated heating/cooling cycles. In each cycle, a sample would be heated past its melting point to 750°C and then quenched using its assigned method. Three trials were performed in order to ensure the repeatability of the methods as well as to maximize thermal contact between the thermocouple and the sample.

Using the modified system, gaseous coolants were found to cool samples at rates up to ~30°C/s while liquid coolants cooled at rates of up to ~500°C/s. The internally cooled geometry imposes directional radially outward progress of the solidification front through the sample. This produces dense samples with no internal shrinkage

porosity. Images from such rapidly cooled microstructures are analyzed in this paper. However, rapid cooling induces vapour film which results in turbulence in liquid coolants, which affects the thermal signal quality. Because of this, thermal analysis, in this paper, is focused on gas-cooled thermal traces in the -15 to -20°C/s range.

## 2.2. Microstructural and microchemical analysis

Solidified cylindrical samples were sectioned normal to the cylinder axis mounted and polished using standard metallographic techniques. At low magnifications, polarized contrast revealed the macro grain structure (Figures 1 and 5). Higher magnifications in an optical microscope revealed the morphology (the shape and distribution) and topology (the connectivity) of dendrite, intermetallic and eutectic structures in the material. These characteristics and the knowledge of the solidification direction allowed for deduction of the phase solidification sequence.

Samples were then imaged in a scanning electron microscope (SEM) equipped with backscatter electron detector (BSD) and an energy dispersive x-ray (EDX) elemental analysis system. Backscatter signal intensity depends on the average atomic number at the electron beam target spot, and thus is quite useful for qualitative phase mapping and identification with sub-nanometer resolution. Conventional quantitative elemental analysis of single-phase materials or large-grained phase aggregates is enabled by the EDX. However, in our rapidly solidified samples, typical constituent size was often sub-micron, which is smaller than the volume in which the characteristic fluorescence x-rays are generated. Consequently, the measured result is a convoluted mixture of the phases sampled by this analytical volume. To resolve this problem, the authors developed a novel EDX result deconvolution technique which depends on taking multiple EDX measurements in a local neighbourhood. This technique assumes that locally each phase has a fixed composition and that the measured results differ in the weight fraction of each phase sampled by the analytical volume of various measurements [11]. These de-convoluted results provided quantitative weight-percent elemental compositions of each observed phase regardless of its size or location, as well as the sample composition expressed in terms of weight fractions of each phase in the local average microstructure. In this paper the authors refer to such sample phase composition as “phase distribution” to clearly differentiate it from the elemental composition of each phase, or average elemental composition of the alloy. Stoichiometry or non-stoichiometry of each phase was deduced from the calculation of atomic fractions of each element in the given phase. These atomic fractions were compared with the literature x-ray diffraction based crystal structure information on phases formed in similar alloys under comparable cooling rates in HP die casting [1].

## 2.3. Cooling curve analysis

A cooling curve is derived from the temperature-time record of the sample being cycled through repeated melting and solidification cycles. To determine the cooling rate, the authors smooth and differentiate the temperature data with respect to time by calculating the slope of a polynomial fit to the data segment adjacent to the point of interest. Even without metallurgical

reactions, the cooling rate becomes less negative as the sample temperature drops, reducing the temperature difference between the sample and the coolant. Therefore the baseline for these metallurgical reaction peaks depends on temperature and is determined by polynomial fits to the data on the plot of cooling rate against temperature. The area of the peaks super-imposed on this sloped baseline represents the enthalpy of solidification of the various solid phases crystallizing out of the melt. To calculate the peak areas one must first calculate the portion of the baseline in the semi-solid region.

### Baseline determination

For the magnesium parent metal, the heat capacities of liquid and solid are different at a melting point. This results in a shift in the baseline between the fully solid and fully liquid regions. At any temperature:

$$B_s/B_l = c_{p_l}/c_{p_s} \quad (1)$$

where  $B_s$  and  $B_l$  are baseline cooling rates (C/s), determined in liquid and solid respectively, and  $c_{p_l}$  and  $c_{p_s}$  are heat capacities of the liquid and solid. Further, in the semi-solid region the baseline value for the semisolid mixture,  $B$ , can be calculated from the respective weight fractions of liquid and solid,  $f_l$  and  $f_s$  as follows:

$$1/B = (1-f_s)/B_l + f_s/B_s \quad (2)$$

The fraction solid at any time is estimated from the fraction of the total thermal solidification peak area that was integrated to that time. Since the peak area depends on the baseline, an iterative solution is required. The procedure is found to converge to a solution after a few iterations. For dilute alloys the problem is simplified by ignoring the contribution of alloying elements to the baseline value.

The  $B_s$  curve is regression fitted to the  $dT/dt$  points at a temperature below the solidus, and constrained to pass through the value of  $B_l * c_{p_l}/c_{p_s}$  at a point selected above the liquidus temperature. The value of  $B_l$  at the selected temperature is determined by the regression fit to the points above the liquidus temperature. The values of  $B_l$  below the selected temperature point are calculated from Equation 1 as  $B_s * c_{p_s}/c_{p_l}$ . The baseline  $B$  for the semi-solid mix is then calculated from  $B_s$  and  $B_l$  by the iterative solution of Equation 2.

Figures 14 and 15 show the cooling rate curves as a function of temperature with the calculated the baseline cooling rate that accounts for the liquid and solid contributions in the semi-solid region for alloys AM60 and AE44 respectively.

### Reaction peak deconvolution

After baseline subtraction the plot of cooling rate against temperature shows a series of convoluted peaks each corresponding to a specific metallurgical reaction. Enthalpy of each reaction is proportional to the area under its own plot of cooling rate against time. Peak deconvolution is necessary to separate the values of interest.

The individual peak baselines are determined by the polynomial fit to the baseline-subtracted data of cooling rate

plotted against temperature. Fitted data is selected adjacent to, but excluding, the temperature range of the peak of interest. The fit interpolates in the temperature range of the peak of interest. In the case of AE44 alloy, solidification started with the formation of AIRE intermetallics, which extended over the temperature range and was not complete when the main  $\alpha$ Mg solidification started. The baseline for the overlapping portion of the AE44 peak was calculated by fitting the low-temperature portion of the  $\alpha$ Mg peak data and forcing the baseline at the start temperature of  $\alpha$ Mg formation to the value that results in a continuous AIRE peak at this temperature after peak baseline subtraction. This procedure is illustrated in Figures 16 and 18.

### Enthalpy calibration

The area of the baseline subtracted peak plotted against solidification time is proportional to the enthalpy of the weight of the solid phase forming during the solidification time interval. The proportionality factor was determined by measuring the peak area for commercially pure Mg, which has a latent heat of solidification of 368 J/g at the melting point as reported by NIST [10]. The calibration is complicated by two facts. First, the measured area of the solidification peak depends on the cooling rate. The area increases as the cooling rate goes more negative. This is most likely an experimental artefact that needs to be calibrated out of the results. The second fact is physically real; the enthalpy of solidification decreases as solidification temperature decreases. This decrease is significant for alloys with a wide solidification temperature range. The calibration measurements in commercially pure Mg spanned a range of  $-2^{\circ}\text{C/s}$  to  $-20^{\circ}\text{C/s}$  for a baseline value during actual solidification. Linear interpolation fit to this data was used to calculate the conversion factor from the area measured in degrees centigrade to energy measured in joules:

$$C2J(T, dT/dt) = \Delta H_m^{\circ}(T)/AP(dT/dt) \quad (3)$$

Here  $\Delta H_m^{\circ}(T)$  is the latent heat of solidification of Mg at temperature  $T$ , and  $AP(dT/dt)$  is the measured area of the  $dT/dt$  peak with baseline subtracted and integrated with respect to time, at a specific baseline cooling rate. The  $\Delta H_m^{\circ}(650^{\circ}\text{C})$  value of  $-348$  J/g for pure Mg was calculated as  $H_f(650^{\circ}\text{C}) - H_s(650^{\circ}\text{C})$  using coefficients of the Shomate equation taken from the NIST chemistry WebBook[11]. The calibrated peak values represent thermal power measured in  $\text{J/s} = \text{W}$  and the integrated area under the peak is the enthalpy of formation of the actual weight of the phase formed measured in J. This weight cannot be estimated directly from the cooling curve analysis, but comes from subsequent microstructural and microchemical analysis of this sample.

### Fraction solid, residual melt and its composition

In the solidification of pure metal, a single phase is formed. In this case, fraction solid at any temperature in the solidification range is:

$$F_s = \int_{T_s}^{T_l} dT/dt \, dt / \int_{T_s}^{T_l} dT/dt \, dt \quad (4)$$

This is the area under the cooling-rate-time peak integrated between  $T_l$  and  $T$  divided by the total peak area integrated between  $T_l$  and  $T_s$ , where  $T_l$  and  $T_s$  are respectively the liquidus and solidus temperatures. This definition holds for any individual phase, but with multiple phases solidifying to produce a compound cooling rate trace, each phase has its own specific enthalpy of formation and weight. Consequently, the fraction solid value needs to be evaluated individually for each phase after deconvolution of baseline subtracted peaks. This individual phase fraction solid information is combined with phase distribution information determined from microchemical analysis results to produce a proper fraction solid curve for the alloy which is typically plotted against temperature. Fraction liquid is the complement:

$$F_l = 1 - F_s \quad (5)$$

The composition of the residual melt can be calculated from the elemental mass balance at each time step. At this point we know the elemental composition and the quantity of each phase coming out of solution at each time step. The authors also know the starting melt composition; hence the residual melt composition is what is left after subtraction of the mass of all elements that went into forming the solid at a particular time step.

The correlation between the cooling curve peaks, the phases observed in the microstructure and their identification is based on the phase quantity and location in the structure and the literature results on phase thermochemical and crystallographic properties and the alloy equilibrium phase diagram [8].

## 3. Experimental results

### 3.1. Alloy AM60B microchemistry

Tables 1 and 2 show the alloy compositions as well as the phase compositions and distributions calculated from SEM-EDX measurements. Directional solidification in radial and outward patterns allowed for identification of the sequence of changes in the alloy and phase composition during solidification.

Table 1 focuses on the AM60B samples solidified at  $-18^{\circ}\text{C/s}$  and  $-280^{\circ}\text{C/s}$ . Phase composition and distributions calculated in this table are later used in calculations of elemental mass balances for cooling trace analysis. For now, it is significant that at  $-18^{\circ}\text{C/s}$  and slower cooling rates the authors observed equilibrium phases in the sample microstructure:  $\alpha$ Mg,  $\text{Mg}_{17}\text{Al}_{12}$ ,  $\text{Al}_8\text{Mn}_5$  and  $\text{Mg}_2\text{Si}$ . At a rapid solidification rate of  $-280^{\circ}\text{C/s}$ , the quantity of intermetallic phases increases by 5 wt% and their composition changes to a metastable structure containing a large excess of Mg.

### 3.2. Alloy AM60B microstructures

Figures 1-4 illustrate the AM60B alloy microstructures and their dependence on the solidification rates. The microstructures are all composed of equiaxed  $\alpha$ Mg grains, and their grain size is only slightly dependent on the cooling rate up to  $-240^{\circ}\text{C/s}$ . Only at  $-280^{\circ}\text{C/s}$  is there significant reduction in grain size. This is correlated with the following findings at  $-280^{\circ}\text{C/s}$ : there is no  $\text{Al}_8\text{Mn}_5$  inside  $\alpha$ Mg grains; the  $\text{Al}_8\text{Mn}_5$  is replaced by metastable Mg-rich  $\text{MgAlMn}$  intermetallics in between the  $\alpha$ Mg grains.



Figure 3 illustrates that as the cooling rate increases  $\alpha$ Mg solidification becomes more dendritic and the grains become equiaxed dendritic rosettes expanding radially out from the central nucleation site.

This implies that at very high cooling rates the nucleation of  $\text{Al}_8\text{Mn}_5$  is suppressed and  $\alpha$ Mg grains nucleate at more abundant nucleation sites, probably small oxide inclusions.

The peak cooling rate is recorded at the start of solidification. As the cooling proceeds, the baseline cooling rate slows down. Figure 2 illustrates how this affects the grain structure in a directionally solidified sample starting at  $-280^\circ\text{C/s}$ . There is noticeable grain coarsening between the start and end regions of the sample (at inner and outer walls).

Figure 4 illustrates how interdendritic melt solidification at the end differs with the cooling rate. At slow cooling rates, equilibrium  $\alpha$ Mg- $\text{Mg}_{17}\text{Al}_{12}$  eutectic forms as a spongy two-phase structure. In the  $-240^\circ\text{C/s}$  and  $-280^\circ\text{C/s}$  samples, the equilibrium phases are replaced by the metastable Mg-rich intermetallics:  $\text{Mg}_x\text{Al}_y$  and  $\text{Mg}_x\text{Al}_y\text{Mn}_z$ .

All these AM60B alloy microstructures tell a story. There is a small but still significant variation in alloy microstructures attributable to the nearly two orders of magnitude change in the solidification rates.

Table 1.  
Comparison of phase compositions and distributions for the rapidly solidified AM60B alloy

Cooling rate: $-18^\circ\text{C/s}$ to $-15^\circ\text{C/s}$					
	AM60B Alloy	$\alpha$ Mg	$\text{Mg}_{17}\text{Al}_{12}$ - $\alpha$ Mg Eutectic	$\text{Al}_8\text{Mn}_5$	$\text{Mg}_2\text{Si}$
Distribution	100.00	86.29	12.92	0.40	0.40
Composition	wt%	wt%	wt%	wt%	wt%
Mg	93.16	97.52	67.10	0.12	63.38
Al	6.26	2.27	32.27	33.58	
Si	0.27	0.07	0.52	0.27	36.62
Mn	0.38	0.14	0.11	60.73	
Fe+Cr+Ni	0.02			5.30	
Cooling rate: $-280^\circ\text{C/s}$					
	AM60B Alloy	$\alpha$ Mg	MgAl IM	MgAlMn IM	$\text{Mg}_2\text{Si}$
Distribution	100.00	81.23	16.68	1.39	0.70
Composition	wt%	wt%	wt%	wt%	wt%
Mg	93.16	97.65	74.26	67.45	63.38
Al	6.26	2.10	25.56	21.12	
Si	0.27	0.01	0.04	0.30	36.62
Mn	0.38	0.24	0.14	11.13	
Fe+Cr+Ni	0.02				

IM - Intermetallic

Table 2.

Comparison of measured area average compositions with those calculated from de-convoluted phase compositions and distribution

AE44 alloy sample solidified at  $240^\circ\text{C/s}$  radially outward in 18-mm diameter, 3-mm wall, hollow cylinder

Area average (wt%)						
	First		Mid-wall		Last	
	Calc.	Meas.	Calc.	Meas.	Calc.	Meas.
Mg	90.21	90.32	87.78	89.34	86.11	86.07
Al	3.26	3.26	3.28	3.28	3.51	3.51
Si	0.11	0.11	0.66	0.10	0.22	0.10
La	1.22	1.22	1.81	1.32	1.38	1.28
Ce	2.63	2.63	2.61	2.63	3.02	2.82
other RE	0.01	0.01	0.02	0.02	0.03	0.03
Zn	0.37	0.37	0.63	0.61	1.12	1.13
Mn	0.32	0.32	0.39	0.37	0.64	0.58
Fe	0.11	0.10	0.29	0.21	0.42	0.43
Cu	0.26	0.30	0.58	0.30	0.50	0.99
Ti	0.07	0.07	0.15	0.10	0.03	0.07

AE44 alloy sample solidified at  $2^\circ\text{C/s}$  radially inward in 18-mm diameter solid cylinder

Area average (wt%)				
Element	First		Last	
	Calc.	Meas.	Calc.	Meas.
Mg	94.94	94.55	95.99	95.35
Al	2.26	2.77	1.91	2.54
Si	0.07	0.08	0.08	0.08
La	0.69	0.69	0.42	0.42
Ce	1.54	1.55	1.14	1.14
Nd	0.38	0.27	0.29	0.22
Mn	0.09	0.10	0.16	0.16
Fe	0.01	0.02	0.01	0.08

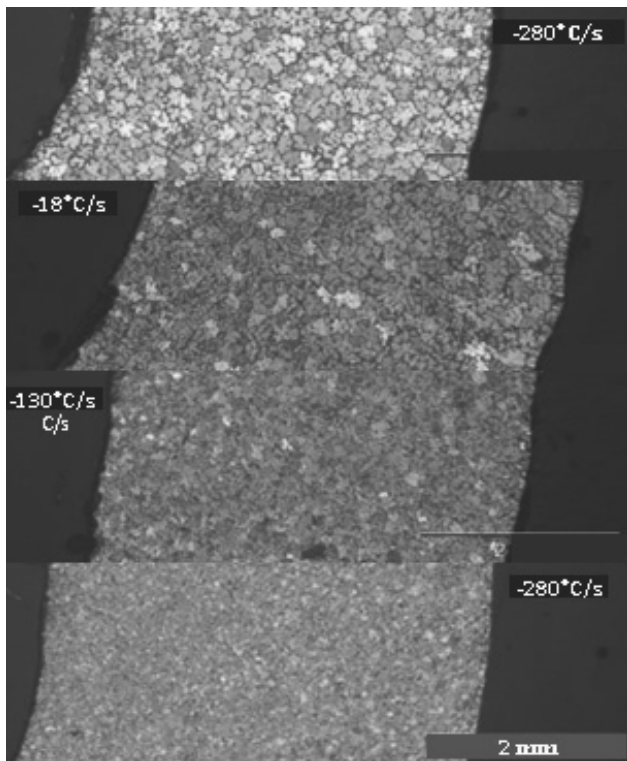


Fig. 1. Alloy AM60B-Dependence of grain size on solidification rate. At  $>20^\circ\text{C/s}$ , the grain structure (equiaxed) and direction (radially outward) are not noticeably affected by the solidification rate. At more rapid rates, grain size decreases and there is a slight size gradient in the solidification direction with grains growing larger later

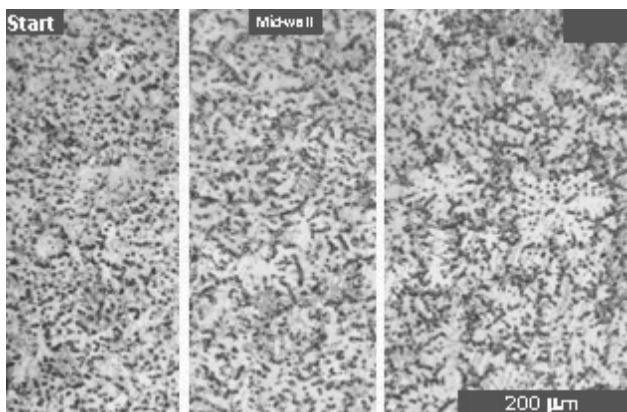


Fig. 2. Alloy AM60B-Comparison of grain size and morphology at the start, centre and end regions for a sample solidified at  $-280^\circ\text{C/s}$ . Images were taken from a polished and etched section accentuating the grain boundaries and inter metalics that are found both inside and between the  $\alpha\text{Mg}$  grains

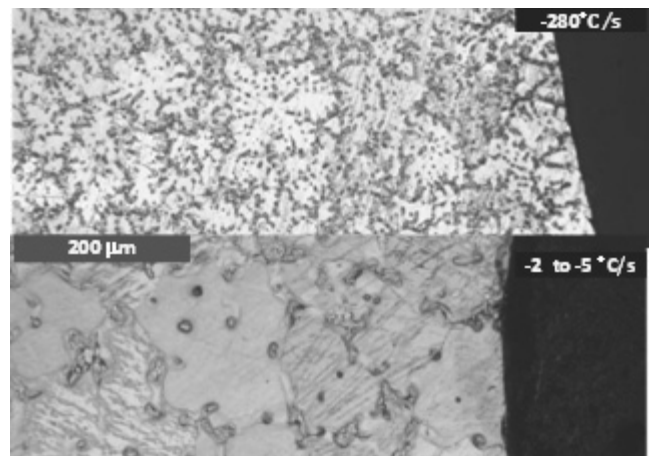


Fig. 3. Alloy AM60B-Comparison of grain morphology in the start region between samples solidified at  $-280^\circ\text{C/s}$  and at  $-2$  to  $-5^\circ\text{C/s}$ . Enhanced tendency for dendritic growth is shown at higher solidification rates. Grains nucleate and grow outward in all directions regardless of the direction of heat extraction. (Sample is cooled from the centre)

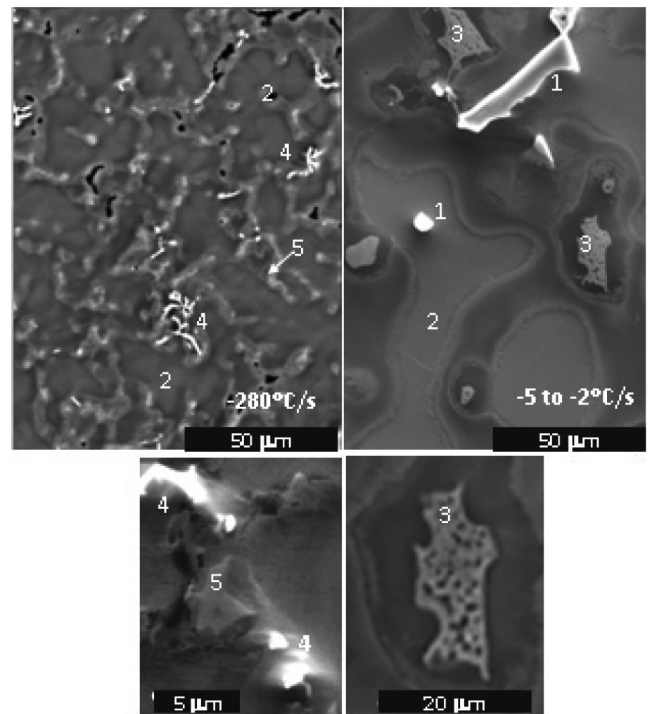


Fig. 4. BSE + SE images of AM60B alloy solidified at  $-280^\circ\text{C/s}$  (left) and  $-5$  to  $-2^\circ\text{C/s}$  (right) showing changes in the microstructure with cooling rate. At  $-5$  to  $-2^\circ\text{C/s}$  the following phases can be observed: blocky  $\text{Al}_8\text{Mn}_5$  (1) inside  $\alpha\text{Mg}$  grains (2) and  $\beta\text{Mg}_{17}\text{Al}_{12}$ - $\alpha\text{Mg}$  eutectic (3) in between, while at  $-280^\circ\text{C/s}$  there is dendritic  $\text{Mg}_x\text{Al}_y\text{Mn}_z$  (4) and single phase  $\text{Mg}_x\text{Al}_y$  (5) in between  $\alpha\text{Mg}$  grain

In all cases the structure is dominated by a nearly equiaxed structure of pretty uniformly sized  $\alpha$ Mg grains. At slow cooling rates one tends to find small dendritic  $\text{Al}_8\text{Mn}_5$  structures inside the  $\alpha$ Mg grains. There are also occasional small equiaxed  $\text{Mg}_2\text{Si}$  crystals located near the grain boundaries but still typically surrounded with  $\alpha$ Mg phase. Between the  $\alpha$ Mg grains there is spongy eutectic structure of  $\beta\text{Mg}_{17}\text{Al}_{12}$  with  $\alpha$ Mg inclusions. At rapid solidification rates between the  $\alpha$ Mg grains, there is a layer of Mg-rich MgAl intermetallic. The grain sizes decreased slightly and the equiaxed  $\alpha$ Mg structures changed from grains to small dendritic rosettes growing out from central  $\text{Al}_8\text{Mn}_5$  intermetallics. At the fastest cooling rate of  $-280^\circ\text{C/s}$ , there is a significant reduction in grain size correlated with the disappearance of the  $\text{Al}_8\text{Mn}_5$  from inside grains.  $\alpha$ Mg grains are now either nucleating homogeneously throughout the melt, or using more abundant smaller oxide particles to nucleate.

### 3.3. Alloy AE44 microchemistry

The first part of Table II focuses on an AE44 sample rapidly solidified at  $-240^\circ\text{C/s}$ . As expected for the case where  $\alpha$ Mg is the first phase to solidify, the Mg concentration in the alloy is highest in the region first to solidify (inner surface) and lowest in the region last to solidify (outer surface). For alloying elements and impurities, the trend is reversed. The concentration of Zn, Mn, Fe and Cu in the alloy all increase locally as the solidification progresses. Results for the slow cooling rate are shown in the second part of Table II. The concentration changes are smaller and the trend is reversed: Mg content increases and the RE element concentration decreases as solidification progresses. This is consistent with topological observations that at the slow cooling rates the AIRE intermetallics start precipitating before  $\alpha$ Mg solidification commences.

Table 2 demonstrates an excellent agreement between the measured area average alloy compositions and the values predicted from the knowledge of the de-convoluted phase compositions and distributions for the samples solidified slowly at  $-2^\circ\text{C/s}$  as well as those quenched at  $-240^\circ\text{C/s}$ . Even though the alloy was nominally the same, it is evident that the two samples had quite different average compositions. The slowly cooled sample averaged  $\sim 95$  wt% Mg, while the quenched one averaged  $\sim 88$  wt% Mg. This is most likely an effect of composition difference between the ingots from which the samples were cut.

Reproducibility of the calculation and some systematic trends with location are evident in the results. There is a systematic reduction in the quantity of  $\alpha$ Mg as solidification progresses, and some transition elements—Zn, Fe, Mn and Cu—increase their concentration in  $\alpha$ Mg as solidification progresses.

The most striking observation is the drastic change in the composition of the  $\text{Al}_x\text{RE}_y$  intermetallic nano-needles and plates which appear morphologically similar in all three regions. The RE elements (Ce, La, Nd and others) substitute for each other in the  $\text{Al}_{11}\text{RE}_3$  and  $\text{Al}_2\text{RE}$  crystal structures. It also appears that under fast cooling rates Mg and Si can substitute for Al. Intermetallics also pick up significant concentrations of transition elements that could either substitute for REs or could form an interstitial solution.

Table 3.

De-convoluted phase distribution and elemental composition (wt%)

AE44 alloy sample directionally solidified across 3-mm cylinder wall at  $-240^\circ\text{C/s}$

(wt%)	$\alpha$ Mg	$(\text{AlMgSi})_x\text{RE}_y$					
		$\text{Al}_{11}\text{RE}_3$	$\text{Al}_3\text{SiRE}_2$	$\text{Al}_2\text{RE}$	$\text{Mg}_2\text{Si}$	$\text{Al}_8\text{Mn}_4\text{RE}$	
Location	first	mid-wall	last	first	mid-wall	last	last
Distrib.	91.54	90.21	89.76	8.46	9.79	9.59	0.51
Mg	97.99	97.30	95.58	5.97	0.04	0.00	60.47
Al	0.32	0.09	0.57	35.15	32.68	30.68	1.74
Si	0.04	0.00	0.03	0.83	6.78	0.14	34.98
La	0.00	0.22	0.19	14.39	16.47	12.55	0.35
Ce	0.40	0.00	0.00	26.77	26.64	31.15	0.50
other RE	0.74	1.17	1.58	8.82	7.74	16.77	0.33
Zn	0.20	0.32	0.85	2.25	3.50	3.64	0.62
Mn	0.10	0.38	0.60	2.73	0.43	0.70	0.12
Fe	0.05	0.22	0.17	0.80	0.98	2.78	0.24
Cu	0.10	0.21	0.40	2.00	3.94	1.44	0.57
Ti	0.05	0.09	0.02	0.29	0.79	0.15	0.09

AE44 alloy 18-mm diameter cylinder solidified radially inward at  $-2^\circ\text{C/s}$

	$\alpha$ Mg		$\text{Al}_2\text{RE}$		$\text{Al}_{11}\text{RE}_3$		$\text{Al}_3\text{SiRE}_2$		$\text{Al}_8\text{Mn}_4\text{RE}$	
	First	Last	First	Last	First	Last	First	Last	First	Last
Distrib.	95.97	97.16	1.94	0.94	0.92	0.27	0.99	1.20	0.18	0.42
Element										
Mg	98.88	98.79	2.42	0.19	0.19	0.19	0.00	0.00	0.42	0.19
Al	1.11	1.17	28.48	29.91	40.92	40.92	20.81	20.10	33.17	33.46
Si	0.01	0.00	0.09	0.00	0.07	0.07	6.64	6.83	0.07	0.12
La	0.00	0.01	9.83	11.72	39.64	39.64	13.01	14.47	3.38	3.35
Ce	0.00	0.00	45.41	46.67	17.57	17.57	46.93	47.39	20.61	20.32
Nd	0.00	0.03	12.86	11.71	0.91	0.91	11.61	10.52	6.56	6.71
Mn	0.00	0.00	0.56	0.00	0.71	0.71	0.51	0.34	34.87	35.12
Fe	0.00	0.00	0.35	0.00	0.18	0.18	0.48	0.35	0.92	0.91

Table 3 shows the results of the phase distribution and composition deconvolution for the quenched sample in the locations near the first, mid-wall and last solidified regions.

Formation of both  $\text{Al}_{11}\text{RE}_3$  and  $\text{Al}_2\text{RE}$  phases has been reported in the Mg alloys. In our case, the stoichiometry of nano-needles and plates shifts from that consistent with substituted  $\text{Al}_{11}\text{RE}_3$  at the start to that consistent with  $\text{Al}_2\text{RE}$  at the end. In the mid-wall region, it is consistent with  $\text{Al}_2\text{SiRE}_2$  composition. All these composition changes occur without major changes in the morphological appearance of these intermetallic nano-particles.

First to solidify when quenched is  $\text{Al}_{11}\text{RE}_3$  heavily substituted with ~6 wt% of Mg. In the mid-wall region, with the local cooling rate reduced by latent heat evolution, the Mg content of the intermetallic decreases but the Si goes up to the point where the intermetallic stoichiometry is  $\text{Al}_3\text{SiRE}_2$ . In the mid-wall region the authors also first see the appearance of isolated blocky AlMn intermetallics that pick up RE elements leading to the stoichiometry of  $\text{Al}_8\text{Mn}_4\text{RE}$ . In the region last to solidify, isolated  $\text{Mg}_2\text{Si}$  intermetallics are added to the structure. Their appearance coincides with the reduction in the Si content of the AlRE intermetallics, which now are close to the Laves phase stoichiometry of  $\text{Al}_2\text{RE}$ .

At the slow cooling rate the intermetallics grew in the melt to a thickness of ~4  $\mu\text{m}$  and diameter of 10-20  $\mu\text{m}$  before they were encased by the solidifying  $\alpha\text{Mg}$  grain. Intermetallics had time to scavenge impurities from the melt, and there was only 1 wt% Al content in the  $\alpha\text{Mg}$  matrix. All the intermetallic phases found in the quenched sample were distinct and easily identifiable at the slow cooling rate. Only  $\text{Mg}_2\text{Si}$  was missing, with all the Si being consumed by  $\text{Al}_3\text{SiRE}_2$  phase.

### 3.4. Alloy AE44 microstructure

Looking at the microstructures of alloy AE44, the authors compared the results obtained for outward directional solidification cooling rates ranging from -22 to -500°C/s and an additional sample air cooled at -2°C/s. Figure 5 shows the macro grain structure of the hollow cylinder wall at the extremes of the cooling rate range. Both have extremely large grains. In the slow cooled sample grains are equiaxed and up to 1 mm in diameter in the mid-wall region. Fast cooling produces elongated grains, some of which span nearly the entire 3-mm wall thickness. There are some smaller grains at both inner and outer surfaces, suggesting preferential heterogeneous nucleation of the grains at the container walls.

Figure 6 depicts the microstructure of the fastest cooled sample in the three locations at the start, mid-wall and at the end. It reveals that the large grains shown in Figure 5 have a dendrite colony substructure with highly aligned dendrite arms. Colonies are predominantly aligned in a radial direction. The dendrite arms are finest at the starting location and are significantly coarser at the end location. At the outer surface there appears to be a 300 $\mu\text{m}$  layer that nucleated at the container surface and grew inwards. This shows the preferential heterogeneous nucleation at the container wall and isolation of the outer region from the inner quenching passage by the latent heat of melt solidification.

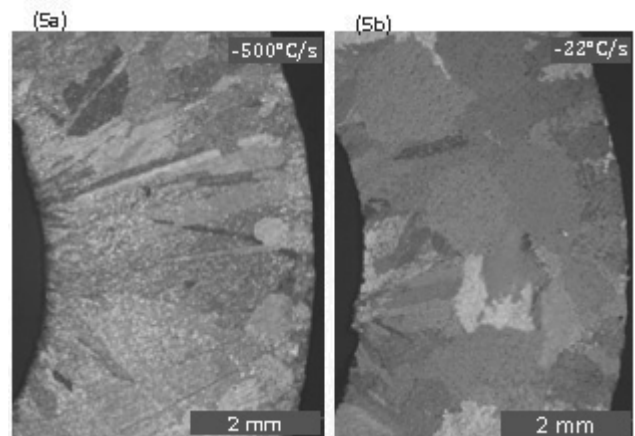


Fig. 5. Alloy AE44-Comparison of grain morphology in samples solidified at -500°C/s (5a, left) and at -22°C/s (5b, right). At -500°C/s, the grains grow radially almost right across the 3-mm wall of the sample. At -22°C/s, the radial, outward grain growth pattern is replaced by extremely large equiaxed grains. In both cases, there appears to be another set of grains that nucleated on the outer surface and grew inward. Hence it appears that there is preferential heterogeneous nucleation on the interface of the boron-nitride coated foil container and very ineffective nucleation in the liquid on the solidifying inter metallic

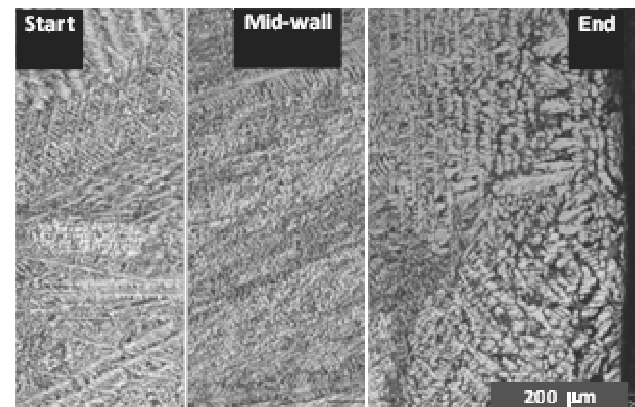


Fig. 6. Alloy AE44-Solidification at -500°C/s reveals that grains are actually large  $\alpha\text{Mg}$  dendrite colonies with dendrite trunks growing in a predominantly radial direction. The nucleation and inward growth of coarse dendrites extends up to ~300 $\mu\text{m}$  from the outer surface

Figure 7 depicts the grain boundary detail in between two large grains in the slowly cooled sample. The grain boundary is jagged and appears to be pinned by the intermetallic particles that are distributed throughout all the grains. This topology implies that the intermetallics precipitated first in the liquid, but did not act as the nucleating sites for the subsequent solidifications of the main  $\alpha\text{Mg}$  grains.

Figure 8, taken from an intermediate -240°C/s, shows the white dendrites to be  $\alpha\text{Mg}$  with the grey intermetallic plates alternating with Mg matrix. This structure implies that at this fast



cooling rate the  $\alpha\text{Mg}$  started solidifying first, and that the intermetallics subsequently precipitated in the interdendritic residual liquid. The final product is a large  $\alpha\text{Mg}$  grain containing the AlRE plates distributed in the former interdendritic spaces.

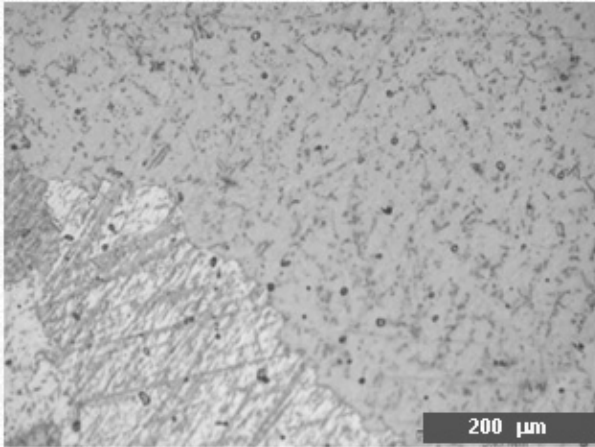


Fig. 7. Alloy AE44-Solidification at  $-22^\circ\text{C/s}$  produces a very tortuous grain boundary between large  $\alpha\text{Mg}$  grains. The grains are full of small inter metalics. This structure implies that the inter metalics precipitated first in the liquid and then the  $\alpha\text{Mg}$  matrix grew among them without nucleating new  $\alpha\text{Mg}$  grains

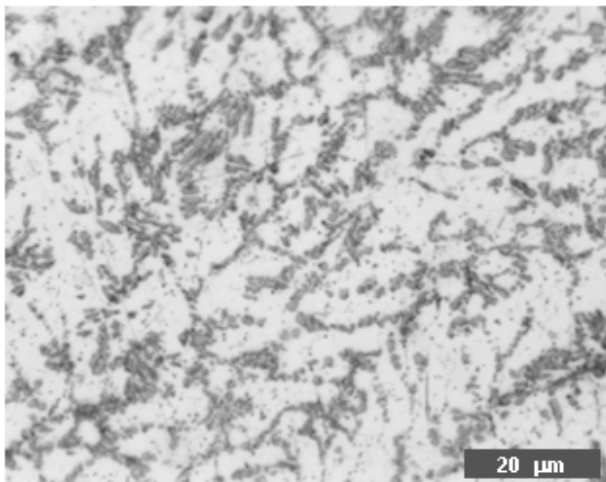


Fig. 8. Alloy AE44- $\text{Al}_{11}\text{RE}_3$  inter metallic plates are seen in this image taken from a sample solidified at  $-240^\circ\text{C/s}$ . There are no grain boundaries separating the  $\alpha\text{Mg}$  dendrites and the inter dendritic material that contains the intermetallic plates. The matrix of the interdendritic material is also  $\alpha\text{Mg}$ . This structure implies that  $\alpha\text{Mg}$  dendrites grew first and then  $\text{Al}_{11}\text{RE}_3$  inter metalics nucleated and grew in the interdendritic liquid, extracting Al and RE metals and allowing  $\alpha\text{Mg}$  to continue growing in between the intermetallic plates without nucleating new  $\alpha\text{Mg}$  grains. The final product is a large  $\alpha\text{Mg}$  grain containing the  $\text{Al}_{11}\text{RE}_3$  plates distributed in the former inter dendritic spaces

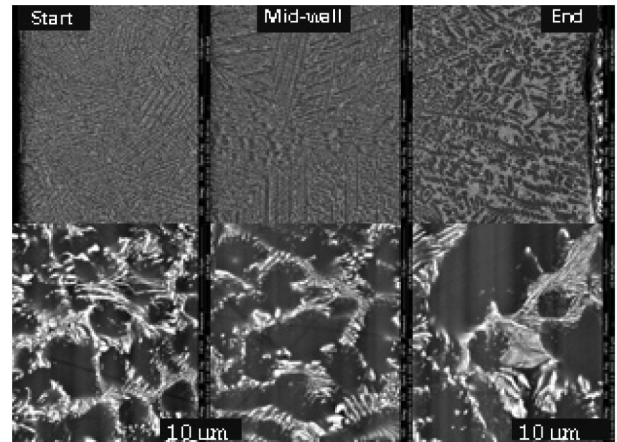


Fig. 9. BSE image of a polished section of AE44 solidified at  $-240^\circ\text{C/s}$ . The release of the enthalpy of formation of the solidifying phases slows down the effective local solidification rate as the solidification proceeds across the sample wall. At the start the dendrites grow preferentially away from the cooled wall. In the mid-wall regions there is random orientation of the dendrite colonies and in the end region, dendrites again nucleate heterogeneously on the container interface and grow inward. The dendrite arm spacing is  $\sim 5\ \mu\text{m}$  at the start,  $\sim 10\ \mu\text{m}$  mid-wall and  $\sim 15\ \mu\text{m}$  at the end

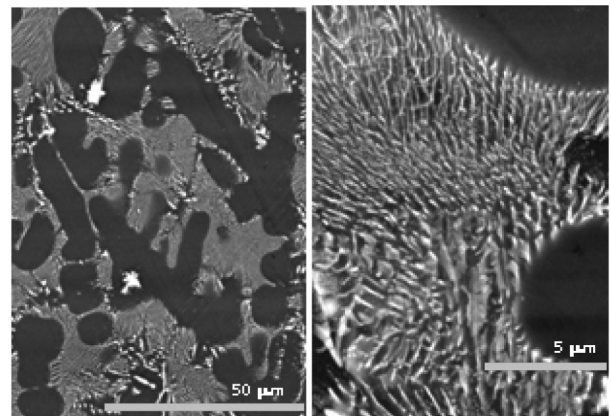


Fig. 10. BSE image of the polished section of AE44 solidified at  $-240^\circ\text{C/s}$  near the solidification end location. Here there are larger  $\alpha\text{Mg}$  dendrites, and a pseudo-eutectic structure of sub-micron  $\text{Al}_{11}\text{RE}_3$  platelets and needles in an  $\alpha\text{Mg}$  matrix. There are also occasional equiaxed blocky  $\text{Al}_8\text{Mn}_4\text{RE}$  intermetallic particles that appear to have precipitated in the residual liquid ahead of the  $\alpha\text{Mg}$  dendrite before the start of the  $\text{Al}_{11}\text{RE}_3$ - $\alpha\text{Mg}$  coupled growth.  $\text{Al}_{11}\text{RE}_3$  crystals appear to be nucleating on the  $\text{Al}_8\text{REMn}_4$  intermetallic particles

Figures 9 and 10 show SEM BSE contrast images of the structure of the same sample in more detail, showing both the needle-like and plate-like morphology of the intermetallics in the interdendritic spaces. At any one location needles and plates

appear to have a similar composition. But, as the microchemical analysis result deconvolution discussed above has shown, this composition changes between the start, mid-wall and the end of solidification regions over a distance of only 3 mm and within a single large  $\alpha\text{Mg}$  grain spanning the wall thickness. The larger bright white blocky particles are  $\text{Al}_8\text{Mn}_4\text{RE}$ . These were occasionally observed at the mid-wall and grew larger and more frequent in the region last to solidify. They appear to have precipitated after the  $\alpha\text{Mg}$ , but before  $\text{AlRE}$ , as the  $\text{AlRE}$  plates appear to nucleate and grow on the  $\text{Al}_8\text{Mn}_4\text{RE}$  particles.

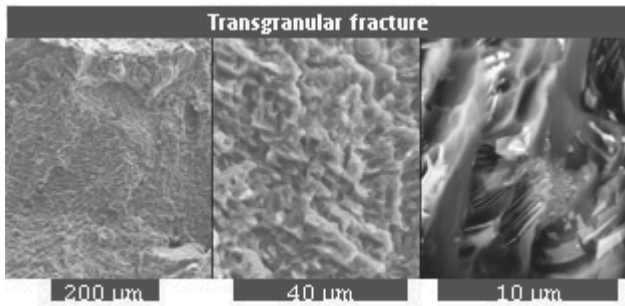


Fig. 11. Fracture surface of AE44 solidified at  $-240^\circ\text{C/s}$ . In the mid-wall region with random alignment of dendrite colonies, fracture is transgranular. A rough fracture surface is produced on a 5- to 10  $\mu\text{m}$  scale characteristic of local dendrite arm spacing. High magnification illustrates plastic flow and necking in  $\mu\text{Mg}$  dendrites and very limited deformation in the interdendritic material reinforced by the  $\text{Al}_{11}\text{RE}_3$  needles and platelets

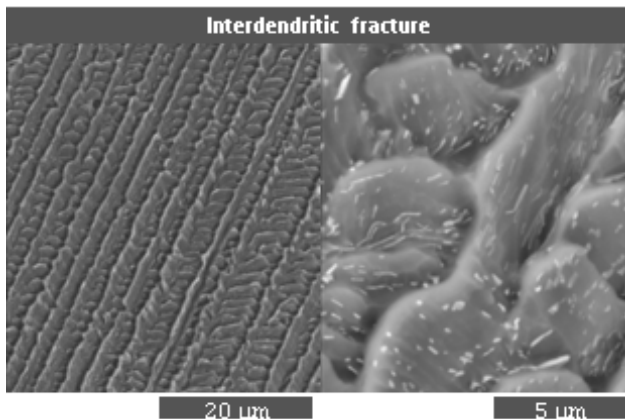


Fig. 12. Fracture surface of AE44 solidified at  $-240^\circ\text{C/s}$ . In this location fracture proceeds along a plane separating two large  $\mu\text{Mg}$  dendrite colonies. From the crystallographic alignment of the dendrite arms and the dendrite cores it can be confirmed that each such colony is a single  $\mu\text{Mg}$  crystal. This mating plane between the two colonies is apparently the weak plane, and shows only minor signs of plastic deformation of dendrite arm surface on sub-micron scale. This plane is locally last to solidify and likely contains fine shrinkage porosity between dendrite arms

$\text{Mg}_2\text{Si}$  blocky particles were also found in the region last to solidify. They are more difficult to spot as there is little BSE contrast between  $\text{Mg}$  and  $\text{Mg}_2\text{Si}$ .

Figure 11 shows a transgranular portion of fracture path through the  $-240^\circ\text{C/s}$  sample. Local ductile deformation and necking is visible in the  $\text{Mg}$  portion, but there is restricted deformation among the intermetallic needles and plates, implying reinforcement. Small size and uniform distributions of the needles and plates suggest particularly effective reinforcement.

Figure 12 shows a fracture path along the grain boundary between two large dendrite colonies. The fracture plane is macroscopically flat, and microscopically reflects the structure of the dendrite arms decorated with the nano-sized  $\text{AlRE}$  intermetallic needles and plates. There is very little evidence of any plastic deformation on the  $\alpha\text{Mg}$  dendrite arms. These grain boundaries appear to be the weak planes in the structure.

The microstructure of the slowly cooled solid cylinder sample of AE44 is shown in Figure 13. It consists of large  $\alpha\text{Mg}$  with well crystallized compact intermetallic crystals distributed throughout the  $\alpha\text{Mg}$  grains.

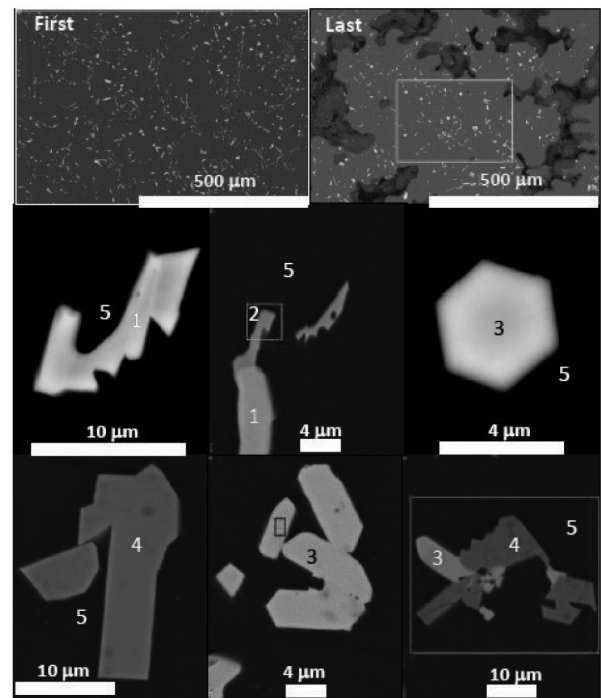


Fig. 13. Backscatter electron contrast images of a polished section of AE44 alloy solidified at  $-2^\circ\text{C/s}$ . Intermetallic particles (1-4) are all embedded in a large  $\alpha\text{Mg}$  grain (5). At the position last to solidify, the dendritic shape of the  $\alpha\text{Mg}$  is revealed by the residual porosity

Phase composition (atomic%)	
$\text{Al}_2\text{RE}$ , Ce rich:	$\text{Al}_{63.6}\text{La}_{4.3}\text{Ce}_{19.5}\text{Nd}_{5.4}\text{Mg}_{6.0}\text{Mn}_{0.6}\text{Fe}_{0.4}$
$\text{Al}_{11}\text{RE}_3$ , La rich:	$\text{Al}_{77.4}\text{Si}_{0.1}\text{La}_{14.6}\text{Ce}_{6.4}\text{Nd}_{0.3}\text{Mn}_{0.6}\text{Fe}_{0.6}$
$\text{Al}_3\text{SiRE}_2$ , hex:	$\text{Al}_{51.3}\text{Si}_{15.4}\text{La}_{6.1}\text{Ce}_{21.8}\text{Nd}_{5.2}\text{Mg}_{0.4}\text{Mn}_{0.6}\text{Fe}_{0.6}$
$\text{Al}_8\text{Mn}_4\text{RE}$ :	$\text{Al}_{59.0}\text{Si}_{0.8}\text{La}_{1.1}\text{Ce}_{6.9}\text{Nd}_{1.1}\text{Mn}_{30.0}\text{Fe}_{0.8}$
$\alpha\text{Mg}$ , large grain:	$\text{Mg}_{99.0}\text{Al}_{1.0}$

The central area last to solidify is spongy revealing the dendritic shape of the growing  $\alpha\text{Mg}$  grains. As was observed at the higher cooling rates, intermetallics were not efficient in nucleating new  $\alpha\text{Mg}$  grains. Three types of AIRE intermetallics were identified and analyzed. These were similar to the compositions of AIRE nano-needles and plates observed in the quenched samples. There was also  $\text{Al}_8\text{Mn}_4\text{RE}$ , but no  $\text{Mg}_2\text{Si}$ . Apparently at the slow cooling rate the Si is all consumed by the  $\text{Al}_3\text{SiRE}_2$  phase. All these intermetallics were in the  $\alpha\text{Mg}$  matrix.

### 3.5. Comparison of AM60B and AE44 alloys

These two alloys show vastly different solidification behaviour. In the case of AM60B, at all but the fastest cooling rates  $\alpha\text{Mg}$  grains nucleated heterogeneously on  $\text{Al}_8\text{Mn}_5$  solid particles dispersed throughout the liquid that precipitated throughout the melt above the nucleation temperature of the  $\alpha\text{Mg}$  phase. Equiaxed growth of these grains produced a uniform microstructure of equiaxed Mg grains that was remarkably insensitive to the solidification rate. An  $\alpha\text{Mg}$ - $\text{Mg}_{17}\text{Al}_{12}$  eutectic structure was found in between the Mg grains.

An increase in solidification rate produced more dendritic looking  $\alpha\text{Mg}$  rosettes, and only at the highest quenching rates did the grain size decrease, presumably due to the reduction in size and an associated increase in the number of available solid nuclei distributed in the melt.

This AM60B behaviour is contrasted with the AE44 alloy where the addition of RE mischmetal suppresses the precipitation of the  $\text{Al}_8\text{Mn}_5$  intermetallics and appears to change the nucleation behaviour of the  $\alpha\text{Mg}$  phase. At slow cooling rates the AIRE intermetallics still precipitate first in the Mg melt, but they are not effective in nucleating the  $\alpha\text{Mg}$ , which then nucleates on the container walls and grows dendritically, forming very large dendrite colonies. At slow cooling rates, isolated intermetallics are dispersed throughout the grains and pin their grain boundaries.

At fast cooling rates, the  $\alpha\text{Mg}$  nucleates and grows first, before the intermetallics which then nucleate and grow in the residual interdendritic liquid. Thermal behaviour, as discussed below, indicates that this precipitation is not associated with an invariant eutectic reaction, in spite of producing needles and plates in the Mg matrix. This structure could easily be interpreted as a product of a eutectic reaction.

Both alloys are well suited to their intended applications. AM60B is commonly used as a die-cast structural alloy. The structure insensitivity to the cooling rate is an advantage in this case, as wall thickness variations within the casting are then less likely to lead to variations in the mechanical properties of the casting. AE44 is designed as a high-temperature creep resistant alloy. The addition of the RE mischmetal ties up Al as HT intermetallics, increases the solidus temperature and suppresses the formation of the lower temperature melting  $\text{Mg}_{17}\text{Al}_{12}$  phase. In the case of directional solidification, the suppression of Mg nucleation on the intermetallics produces large dendritic colonies reminiscent of single crystal superalloy microstructures favoured for creep-resistant HT turbine blade applications. At high cooling rates these large dendrite colonies are efficiently reinforced by nano-sized AIRE needles and plates distributed between each small dendrite arm. Rapidly solidified AE44 seems to be very well suited for elevated temperature creep resistant service.

### Comparison of thermal analysis of AM60B and AE44 alloys

The authors used the above microstructural and microchemical information in the interpretation of the thermal analysis results. Microstructure topology establishes the solidification sequence. At a cooling rate of  $\sim 20^\circ\text{C/s}$  for AM60B it is: 1.  $\text{Al}_8\text{Mn}_5$ ; 2.  $\alpha\text{Mg}$ ; 3.  $\text{Mg}_2\text{Si}$ ; and finally 4.  $\text{Mg}$ - $\text{Mg}_{17}\text{Al}_{12}$  eutectic. For AM60B, this sequence does not appear to change at higher cooling rates. For AE44, at  $\sim 20^\circ\text{C/s}$ , the solidification initiation sequence is: 1.  $\text{Al}_x\text{RE}_y$ ; 2.  $\alpha\text{Mg}$ ; 3.  $\text{Al}_3\text{SiRE}_2$ ; 4.  $\text{Al}_8\text{Mn}_4\text{RE}$ . The solidification range of  $\alpha\text{Mg}$  is wider than that of the intermetallics and it appears to be the phase that completes the sequence. At cooling rates  $< 200^\circ\text{C/s}$  this sequence changes to: 1.  $\alpha\text{Mg}$ ; 2.  $\text{Al}_{11}\text{RE}_3$ ; 3.  $\text{Al}_3\text{SiRE}_2$ ; 4.  $\text{Al}_2\text{RE}$ ; 5.  $\text{Al}_8\text{Mn}_4\text{RE}$ ; with  $\alpha\text{Mg}$  also completing the sequence. At both high and low cooling rates the intermetallic formation exotherms are expected to overlap the main  $\alpha\text{Mg}$  solidification thermal peak.

Deconvolution of the microchemical analytical data provides both the composition and the abundance (the distribution) of each phase in the microstructure. These are given in Tables 1-3 above.

Thermal analysis then matches this microstructural data with de-convoluted and calibrated cooling rate peaks to extract the following information.

### Cooling rate-temperature curves

Plotting the cooling rate against temperature for the solidification of the 5.7-g 18-mm OD, 3-mm wall, hollow cylinder samples, allows for the visualization of the exotherms during solidification. These plots are then used to fit and subtract the baseline and then to de-convolute individual thermal peaks that need to be correlated with the phase solidification sequence and phase abundance determined above.

Figures 14 and 15 compare the curves for the cooling rate plotted against temperature for the AM60B and for the AE44 solidified at  $\sim 20^\circ\text{C/s}$ . For both alloys, the main  $\alpha\text{Mg}$  peak has a maximum at  $\sim 630^\circ\text{C}$ , but the solidification range is quite different. The solidus for the AE44 is at  $557^\circ\text{C}$ , with no final eutectic exotherm, while solidification continues until  $440^\circ\text{C}$  for AM60B, with a very sharp  $\text{Mg}_{17}\text{Al}_{12}$  exotherm at that point.

In both alloys there is precipitation occurring in the melt above the  $\alpha\text{Mg}$  nucleation temperature. For the AM60B, the  $\text{Al}_8\text{Mn}_5$  precipitates around  $680^\circ\text{C}$  and its formation is complete by the time  $\alpha\text{Mn}$  nucleates and  $\text{Al}_8\text{Mn}_5$  is then able to provide solid particles uniformly distributed throughout the melt as a substrate for heterogeneous nucleation. For the AE44, AIRE intermetallic precipitation begins at  $660^\circ\text{C}$  and continues strongly, while  $\alpha\text{Mg}$  nucleates on the cylinder inner surface and grows radially outwards encasing the pre-existing intermetallics in the  $\alpha\text{Mg}$  grains.

The expected shape of the  $\alpha\text{Mg}$  solidification peak is well illustrated in the AM60B graph (Figure 14) where there is no thermal interference from intermetallic formation. This shape is characterized by a steep rise to a peak maximum followed by an almost equally steep drop immediately thereafter.

The exothermic effect of continuing intermetallic formation in AE44 is seen as a significant broadening of the top of the  $\alpha\text{Mg}$  peak (Figure 15).



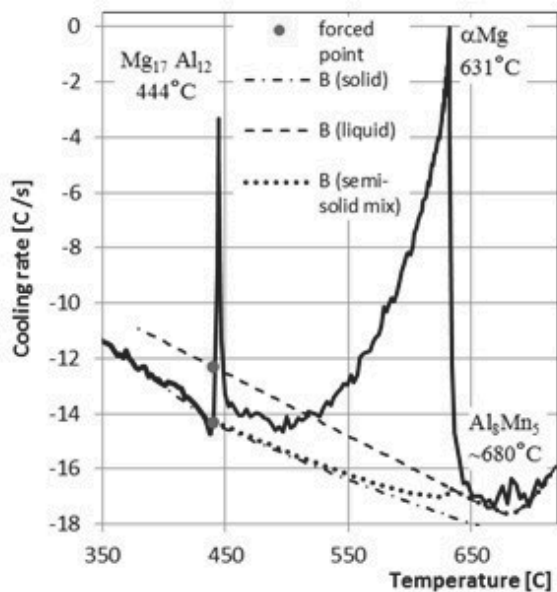


Fig. 14. The AM60B alloy cooling curve with calculated baseline. The liquid baseline is extrapolated linearly to a point located at the solidus temperature and a value given by Equation 1. The solid baseline is extrapolated to the liquidus temperature based on Equation 1 and the interpolated value of the liquid baseline. The semi-solid mix baseline is calculated from the solid and liquid baselines according to Equation 2

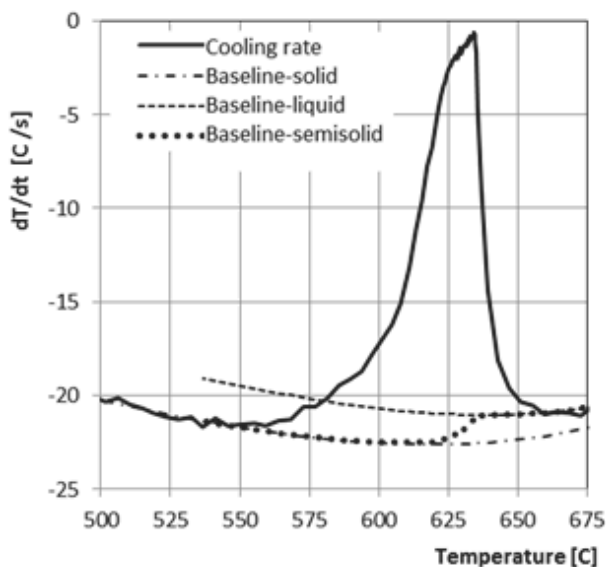


Fig. 15. Cooling rate-temperature plot with baseline for AE44 solidified at  $-22^{\circ}\text{C}$

This interpretation allows for the deconvolution of the overlapping  $\alpha\text{Mg}$  and intermetallic peaks. Deconvolution is done

by fitting the tail of the baseline subtracted peak ( $<600^{\circ}\text{C}$ ) to a polynomial that is forced to intersect the rising edge of the peak at a value that produces a smoothly continuous curve for the intermetallic peak. Figure 16 illustrates that after baseline subtraction the intermetallic peak is smooth and nearly Gaussian in shape starting at  $650^{\circ}\text{C}$ , maximum at  $625^{\circ}\text{C}$ , and ending at  $600^{\circ}\text{C}$ . The  $\alpha\text{Mg}$  peak initiates at  $\sim 640^{\circ}\text{C}$ , rises sharply to maximum at  $635^{\circ}\text{C}$ , and then decays smoothly to a solidus temperature of  $\sim 557^{\circ}\text{C}$ , a range of only  $83^{\circ}\text{C}$ . The metallography and microchemical analysis identified four separate intermetallic species, all co-precipitating in the melt in a sequence based on the topology and the location in the sample wall. The authors can see only a single strong intermetallic thermal signature and cannot separate the contribution of the individual species. The strength and simultaneity of the intermetallic formation exotherm suggests a reason for the observation of the lack of nucleation of new  $\alpha\text{Mg}$  grains on the growing intermetallic crystals. The authors postulate that the heat released by the intermetallic formation increases the temperature of the intermetallic particle and its local surroundings, whereas the nucleation requires under cooling which cannot be found on the actively growing intermetallic crystals.

#### The latent heat of alloy solidification and the energy of component phase formation

The latent heat of alloy solidification is calculated by the integration of the area under the curve of cooling rate against time and dividing it by the total alloy sample weight. The curve is calibrated to power units (Watts) by performing a similar solidification experiment with pure Mg, which has a known latent heat of fusion of  $368\text{ J/g}$  at  $650^{\circ}\text{C}$ .

The energy of component phase formation is calculated by finding the area under the de-convoluted individual phase peaks plotted against time, and dividing that calibrated energy by the weight of each component phase. These weights are calculated from the sample weight multiplied by the phase distribution fraction for the phase of interest. The phase distribution is determined by deconvolution of the microchemical analysis results.

Figures 16 and 17 compare the graphs of exotherm power plotted against time for AM60B and AE44. In the AM60B, the individual peaks are nearly not overlapping and only the  $\text{Mg}_2\text{Si}$  peak requires deconvolution from the tail of the  $\alpha\text{Mg}$  peak.

The resulting calculated latent heat of AM60B alloy solidification and the heats of formation of the  $\text{Al}_8\text{Mn}_5$ ,  $\text{Mg}_2\text{Si}$  and  $\text{Mg}_{17}\text{Al}_{12}$  intermetallics are given in Table IV.

The power-time graph for AE44 in Figure 17 is quite different. It is almost a rectangular pulse of  $\sim 20\text{W}$  for the entire solidification time, yielding an area of  $348\text{ J/g}$  for the latent heat of AE44 formation. The curve of cooling rate against time in Figures 18 and 19 show the deconvolution into  $\alpha\text{Mg}$  and intermetallic contributions. The calibrated areas under the component peaks yield the heat of formation of the  $\alpha\text{Mg}$  phase in AE44 and the weighted average of the heats of formation of the intermetallic component phases included in Table 4.



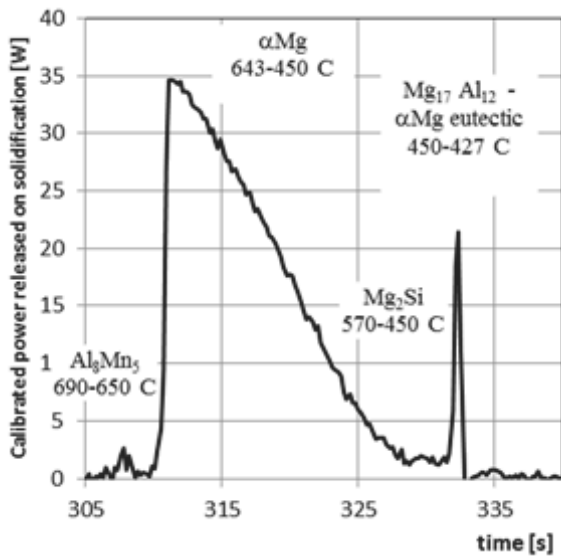


Fig. 16. Calibrated values of the power released during solidification of a 5.7-g AM60B alloy sample at  $-18^{\circ}\text{C/s}$  to  $-15^{\circ}\text{C/s}$ . Integration of the individual peak areas yields experimental values for enthalpy of formation. For AM60B the phase formation is sequential:  $\text{Al}_3\text{Mn}_5$ ,  $\alpha\text{Mg}$ ,  $\text{Mg}_2\text{Si}$  and  $\text{Mg}_{17}\text{Al}_{12}\text{Mg-Mg}$  eutectic

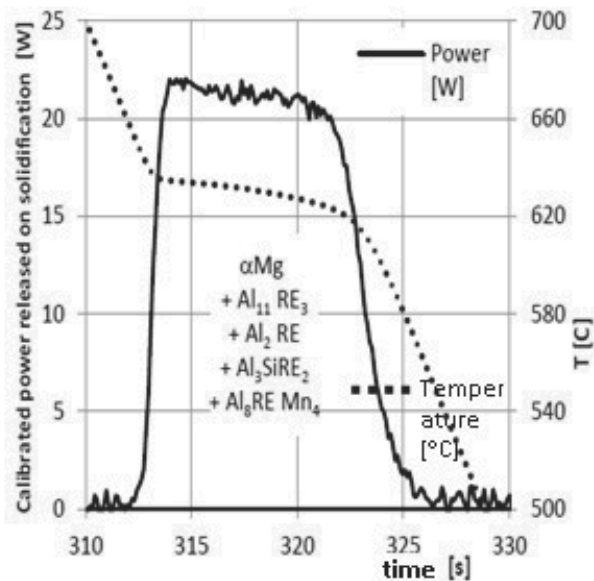


Fig. 17. Calibrated values of the power released during solidification of a 5.7-g AE44 alloy sample at  $-22^{\circ}\text{C/s}$ . Attribution of energy to individual phases is not feasible based on this data. Latent heat of solidification of the AE44 alloy is the area under the power curve,  $-348\text{ J/g}$ . This is significantly more exothermic than AM60B, implying that formation of the AIRE intermetallics is highly exothermic

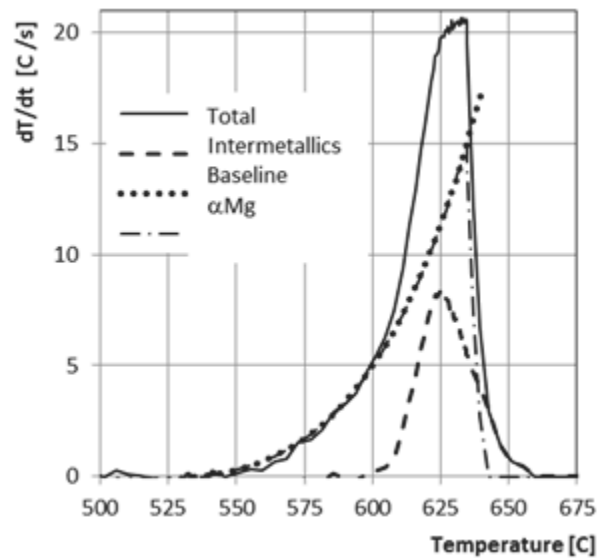


Fig. 18. Baseline subtracted and de-convoluted cooling rate peaks as a function of temperature for AE44 solidified at  $-22^{\circ}\text{C/s}$

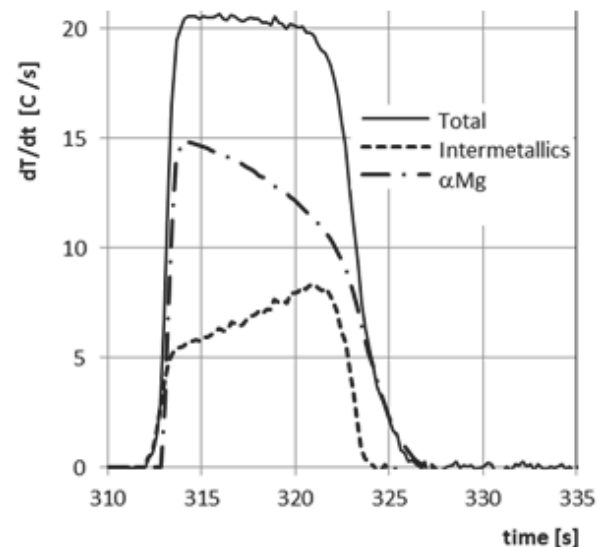


Fig. 19. Thermal power released as a function of time by solidification of a 5.7-g AE44 at  $-20^{\circ}\text{C/s}$ . For AE44 phase formation is simultaneous for  $\alpha\text{Mg}$  and the various intermetallic. De-convolution of the contributions of  $\alpha\text{Mg}$  and the combined intermetallics was performed

#### The fraction solid and liquid of the alloy and fraction solid of individual phases as a function of temperature

Decomposition of the thermal trace into energy contributions of individual phase peaks and association of these contributions with the phase distribution determined by microchemical analysis

allowed the authors to properly identify the individual phase contributions to the fraction solid during the solidification event.

Figures 20 and 21 compare these fraction solid and fraction liquid curves for AM60B and for AE44. In the case of AM60B,  $\text{Al}_8\text{Mn}_5$  contributes 0.3wt% between 687°C and 650°C,  $\alpha\text{Mg}$  contributes 85% between 643°C and 450°C and  $\text{Mg}_2\text{Si}$  0.3% between 475°C and 450°C. The final  $\alpha\text{Mg}$ - $\text{Mg}_{17}\text{Al}_{12}$  “eutectic” solidification contributes 12% between 450°C and 428°C. This contrasts with a much simpler graph for AE44. Here only 0.3 wt% of intermetallics has solidified between 640°C and 635°C when  $\alpha\text{Mg}$  nucleates. Both continue solidifying simultaneously to 600°C, at which temperature intermetallic formation is complete at 12% and  $\alpha\text{Mg}$  reaches 85%. Solidification of the residual liquid produces additional 3% of  $\alpha\text{Mg}$  before the alloy solidification process reaches solidus at 557°C.

Table 4.  
Enthalpy of formation of intermetallic phase

AM60B melt solidifying at -18°C/s				
	Alloy latent heat	$\alpha\text{Mg}$	$\text{Mg}_{17}\text{Al}_{12}$ - $\alpha\text{Mg}$ eutectic	$\text{Al}_8\text{Mn}_5$
$\Delta H_f$ [J/g]	-289	-317	-79	-535
$T_{\text{start}}$ [°C]	697	647	452	697
$T_{\text{max}}$ [°C]	632	632	445	683
$T_{\text{end}}$ [°C]	441	452	441	654

AE44 melt solidifying at -21°C/s		
	Alloy latent heat	$\alpha\text{Mg}$
$\Delta H_f$ [J/g]	-359	-264
$T_{\text{start}}$ [°C]	660	640
$T_{\text{max}}$ [°C]	635	635
$T_{\text{end}}$ [°C]	657	657

## 4. Discussion

Work reported here gave an insight to the effect of solidification rate on the as-cast microstructure, phase composition and solidification sequence for two structural Mg casting alloys-AM60B and AE44. The results were drastically different for the two alloys, yet it can be argued that each is well suited to its target application. The grain size of AM60B is quite insensitive to the solidification rate, a fact that should make the mechanical properties of the casting mostly independent of the variation in the wall thickness of the casting. This feature is quite desirable for structural die castings-a major market for the AM60B alloy.

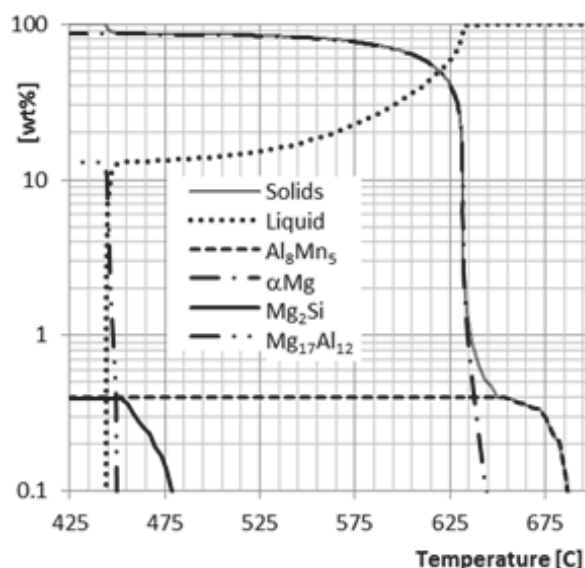


Fig. 20. AM60B alloy phase evolution during solidification at -18°C/s to -14°C/s. The solid forms as 0.3% of  $\text{Al}_8\text{Mn}_5$  between 687°C and 650°C; 85% as  $\alpha\text{Mg}$  between 643°C and 450°C and finally as 12% of  $\text{Mg}_{17}\text{Al}_{12}$ - $\alpha\text{Mg}$  eutectic between 450°C and 428°C

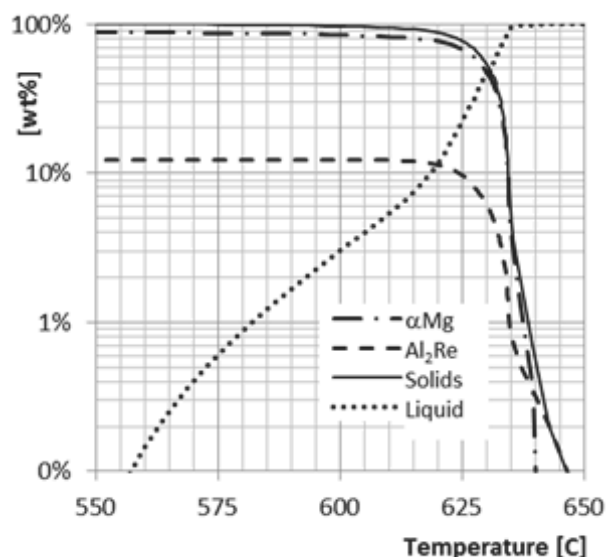


Fig. 21. Fraction solid of individual phases during solidification of AE44 alloy at -21°C/s. There is a very narrow solidification range between 640°C and 600°C. At this relatively low solidification rate AIRE intermetallics precipitate first in the liquid, and this intermetallic formation continues simultaneously with solidification of  $\alpha\text{Mg}$  between 630°C and 600°C, where it reaches 12% intermetallic content. Solidification of the residual melt produces 3% more  $\alpha\text{Mg}$  before the process is complete at 557°C

This contrasts with AE44, whose structure is dominated by very large  $\alpha$ Mg dendrite colonies. Such a structure is desirable for elevated temperature creep resistant applications. These dendrite colonies are internally reinforced by in-situ precipitated intermetallics. The authors demonstrated that the structure of these intermetallics is critically determined by the cooling solidification rate. Fast, directionally quenched samples contained 12% of intermetallic needles and plates with 100 nm diameter or plate thickness. Such fine reinforcements inside grains that span nearly the entire wall thickness of the casting promise quantum improvement in the desired HT creep resistance.

In performing this work, the authors significantly advanced the testing and analytical techniques for both microchemical analysis and thermal analysis of macro samples produced by the UMSA Technology Platform.

## 5. Conclusions and future work

The UMSA Technology Platform has been modified to enable solidification of alloy melts at cooling rates up to  $-500^{\circ}\text{C/s}$ .

A combination of cooling curve analysis with microstructural and microchemical results yields a wealth of information on the phases formed, sequence of events, the enthalpies of formation of component phases and evolution of residual melt composition during solidification.

Reliable and reproducible cooling curves were obtained with sufficient detail to resolve the component phase contributions at cooling rates up to  $-20^{\circ}\text{C/s}$  for the AM60B alloy.

The AE44 alloy has such a narrow solidification range that even at slow cooling rates individual phase contributions are not resolved in the cooling curves. Nevertheless, the current work demonstrated that more rapid solidification can alter the phase solidification sequence and can significantly affect the alloy microstructure.

At very rapid solidification rates, detail is lost from the cooling traces due to a combination of actual change in the type and quantity of phase formed, as well as to experimental limitations. Future work will focus on eliminating the experimental limitations and extending the cooling rate range over which reliable, quantifiable results can be obtained.

## Acknowledgements

This research was partially funded by AUTO21, a member of the Networks of Centres of Excellence of Canada program. An NSERC Discovery Grant and CanmetMATERIALS also partially funded this research. The GCI contribution was partially funded by

the Canadian SR&ED program. Assistance from Sharon Lackie in the analysis of samples is also gratefully acknowledged.

## References

- [1] A. Kielbus, Microstructure of AE44 magnesium alloy before and after hot-chamber die casting, *Journal of Achievements in Materials and Manufacturing Engineering* 20/1-2 (2007) 459-462.
- [2] T. Rzychoń, A. Kielbus, J. Cwajna, J. Mizera, Microstructural stability and creep properties of die casting Mg-4Al-4RE magnesium alloy, *Materials Characterization* 60 (2009) 1107-1113.
- [3] J.P. Weiler, J.T. Wood, R.J. Klassen, R. Berkmortel, G. Wang, Variability of skin thickness in an AM60B magnesium alloy die-casting, *Materials Science and Engineering* 419 (2006) 297-305.
- [4] T. Rzychoń, A. Kielbus, The influence of wall thickness on the microstructure of HPDC AE44 alloy, *Archives of Materials Science and Engineering* 28/8 (2007) 471-474.
- [5] W. Huang, B. Hou, Y. Pang, Z. Zhou, Fretting wear behaviour of AZ91D and AM60B magnesium alloys, *Wear* 260 (2006) 1173-1178.
- [6] E.W. Jarfors, K.-U. Kainer, M.-J. Tan, J. Yong, Recent developments in the manufacturing of components from aluminium-, magnesium- and titanium-based alloys, *COSMOS* 5/1 (2009) 23-58.
- [7] J. Gesing, N.D. Reade, J.H. Sokolowski, C. Blawert, Solidification behaviour of recyclable Mg alloys-AZ91 and AZC1231, magnesium technology, *The Minerals, Metals & Materials Society* (2009) 117-128.
- [8] D. Mirković, R. Schmid-Fetzer, Solidification curves for commercial Mg alloys determined from differential scanning calorimetry with improved heat-transfer modeling, *Metallurgical and Materials Transactions A* 38A (2007) 2575-2592.
- [9] J. Zhang, K. Liu, D. Fang, X. Qiu, D. Tang, J. Meng, Microstructure, tensile properties, and creep behaviour of high-pressure die-cast Mg-4Al-4RE-0.4Mn (RE = La, Ce) alloys, *Journal of Materials Science* 44/8 (2009) 2046-2054.
- [10] NIST Chemistry WebBook, <http://webbook.nist.gov/chemistry/>.
- [11] A.J. Gesing, P. Marchwica, S. Lackie, J. Sokolowski, Quantitative X-ray fluorescence determination of elemental composition of micro-constituents smaller than the electron probe volume, *Proceedings of the Characterization of Minerals, Metals and Materials Symposium TMS'2013, San Antonio, 2013*, 79-90.